DESIGN OF A WIND TUNNEL MODEL FOR A REUSABLE LAUNCH VEHICLE DURING ITS LANDING BURN

Anh Tuan Hoang[1], Nicholas J. Lawson[1] & Tamas Bykerk[2]

[1]The University of Sydney, New South Wales, Australia
[2]German Aerospace Center (DLR), Goettingen, Germany

Abstract

This paper outlines the design process for a wind tunnel model of a reusable launch vehicle (RLV) during its landing burn. The development of the model occurs in three main phases. Initially, the design is created based on assumed nozzle flow conditions, ensuring that the key parameters of the testing conditions are matched with those of the flight conditions. Subsequently, the prototype is printed and used to measure the actual nozzle flow conditions using a newly developed measurement system. Upon acquiring the actual parameters, the model is finalised, featuring a nozzle throat diameter of 5 mm, an expansion ratio of 1.115, a base diameter of 21 mm, and a length of 300 mm. This model satisfies the retropropulsion similarity criteria with an aerodynamic thrust coefficient $C_T = 124.4$ and an ambient pressure ratio $APR = 0.762$. CFD simulations are used to complement experimental data and examine the flowfield around the wind tunnel model. It was observed that a supersonic jet is achieved and a large recirculation region forms along its length.

Keywords: Retropropulsion, Aerodynamics, Reusable Launch Vehicle, Landing Burn

1. Introduction

The concept of reusing rockets, either fully or partially, dates back to the Apollo designs of Wernher von Braun in the 1960s [1]. Initially, RLVs were more expensive than Expendable Launch Vehicles (ELVs) such as Saturn V or Soyuz, mainly due to NASA's experience with the Space Shuttle Program [2]. However, SpaceX has made great strides in RLVs, reducing the cost of space travel by reusing some of the launcher components. The SpaceX Falcon 9, a two-stage vertical takeoff, vertical landing (VTVL) launch vehicle powered by liquid oxygen (LOX) and rocket-grade kerosene (RP-1) [3], has revolutionised the aerospace industry, leading to a significant decrease in space launch costs. The design of RLVs is complicated due to the wide range of flight conditions and the effects of retropropulsion [4]. Wind tunnel experiments are a valuable tool when attempting to better understand the aerodynamic properties of RLVs in different flight phases. This paper focusses on designing a wind tunnel model to be tested under subsonic conditions representative of the landing phase of flight. The trajectory and geometry are based on the RFZ vehicle, a recently published, open source configuration, similar to the Falcon 9 [5].

2. Design Methodology

When modelling rocket engines in retropropulsion, the ambient pressure ratio APR and the thrust coefficient C_T are the two important scaling parameters that characterise the retropropulsion phenomenon [6]. The ambient pressure ratio APR, which is the ratio between the nozzle exit pressure p_e and freestream pressure p_∞, is given by:

$$APR = \frac{p_e}{p_\infty} \tag{1}$$

The thrust coefficient C_T can be determined from freestream Mach number M_∞, ambient pressure ratio APR, nozzle geometry and propellant gas [7] as:

$$C_T = \frac{2}{\gamma_\infty M_\infty^2}\frac{p_e}{p_\infty}\frac{A_e}{A_B}(1+\gamma_e M_e^2) = \frac{2}{\gamma_\infty M_\infty^2} APR \frac{\varepsilon A_*}{A_B}(1+\gamma_e M_e^2) \tag{2}$$

Furthermore, the expansion ratio ε of the aerodynamic model in testing condition can be written in term of nozzle exit Mach number M_e, nozzle throat area A_* and rocket base area A_B as [8]:

$$\varepsilon = \frac{1}{M_e}\left[\frac{2}{\gamma_\infty+1}\left(1+\frac{\gamma_\infty-1}{2}M_e^2\right)\right]^{\frac{\gamma_\infty+1}{2(\gamma_\infty-1)}} \tag{3}$$

The model nozzle throat was estimated from estimated flow conditions, that the compressed air supply can provide, ensuring that the converging-diverging nozzle is choked at the throat. Assuming that the compressed air supply can provide a total pressure of $p_{t,wt} = 400000$ Pa at a total temperature of $T_{t,wt} = 300$ K, and a mass flow rate of $\dot{m}_{cc,wt} = 300$ SLPM $= 6.125 \times 10^{-3}$ kg/s, the nozzle throat area can be determined as [9]:

$$A_* = \frac{\dot{m}_{cc,wt}\sqrt{T_{t,wt}}}{p_{t,wt}}\sqrt{\frac{R}{\gamma_\infty}}\left(\frac{\gamma_\infty+1}{2}\right)^{\frac{\gamma_\infty+1}{2(\gamma_\infty-1)}} = 6.56\times10^{-6}\ \text{m}^2 \tag{4}$$

To determine the expansion ratio ε, the scaling parameters of testing conditions are matched with those of the given flight conditions during landing burn [10]. For the current model, if both ambient pressure ratio APR and freestream Mach number M_∞ are matched, the thrust coefficient C_T of testing conditions will be too small compared to that of flight conditions. Given that $M_\infty << 0.3$ under both flight and testing conditions, the freestream flow is incompressible [11], and therefore it can be assumed that the freestream velocity of the testing conditions can be adjusted to match C_T without significantly affecting the flow characteristics. As a result, the values C_T in two conditions are matched by varying M_∞ of testing conditions, as shown in Figure 1.

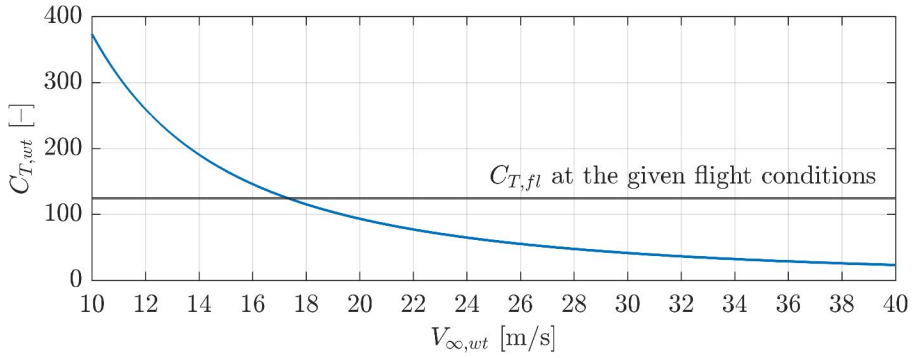

Figure 1 – The variation of $C_{T,wt}$ as a function of $V_{\infty,wt}$

The primary parameters for wind tunnel testing conditions are derived for the initial design and compared with flight conditions, as shown in Table 1.

Condition	C_T [–]	APR [–]	V_∞ [m/s]	p_∞ [Pa]	T_∞ [K]	ε [–]	p_e [Pa]	M_e [–]	T_e [K]
Flight	124.4	0.762	32.22	100300	287.5	16	76460	3.521	1810
Testing	124.4	0.762	17.34	101300	288	1.368	77250	1.732	187.5

Table 1 – The main configurations of the flight and testing conditions for the initial design

It can be seen from Table 1 that the primary similarity parameters C_T and APR of the two conditions are matched, ensuring that the experiments can effectively represent the subsonic retropropulsion during the landing burn. Although there is a difference in the freestream velocity V_∞ between the two conditions, they both involve low-speed, incompressible flows, ensuring a high level of similarity in freestream conditions. Finally, the nozzle exit temperature $T_e = 187.5$ K is sufficiently high to prevent condensation at the nozzle exit [12].

3. Nozzle Parameter Measurement Setup

3.1 Measurement System and Calibrations

To obtain the actual nozzle flow parameters, the initial design is printed and tested. The high pressure conditions within the nozzle present difficulties in measuring flow parameters, as the existing Scanivalve pressure scanner [13] in the wind tunnel lab is inadequate. Furthermore, apart from pressure, the measurement of the mass flow rate is crucial to a complete definition of the flow parameters in the nozzle. Consequently, a new measurement system needs to be developed to accurately capture the internal flow conditions of the nozzle.

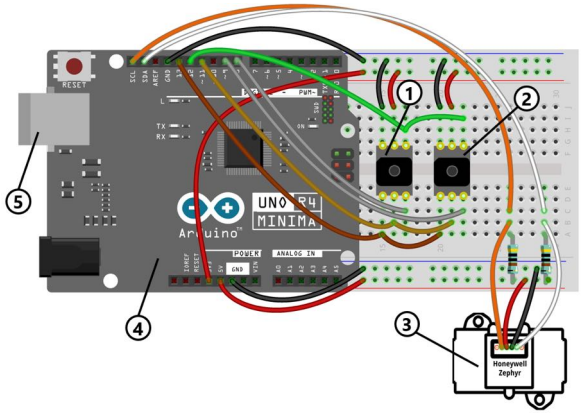

Figure 2 – The circuit schematic for the nozzle parameter measurement system
1, 2 - Honeywell pressure sensors; 3 - Honeywell Mass Flowmeter;
4 - Arduino Uno R4 Minima microcontroller, 5 - USB-C port

The measurement system uses a Honeywell Zephyr thermal mass flowmeter [14] and Honeywell ABP2 pressure sensors [15] to measure mass flow rate and static pressure, respectively. The flowmeter operates within a range of 0 to 300 SLPM and a temperature range of 0 to 50 ℃, while the pressure sensors, made of piezoresistive silicon, measure pressures up to 150 psig with a total error band of 1.5%. Data from these sensors are transmitted to an Arduino Uno R4 Minima microcontroller [16], which then relays the information to a computer via USB-C. The wiring diagram for nozzle parameter measurement system is illustrated in Figure 2.

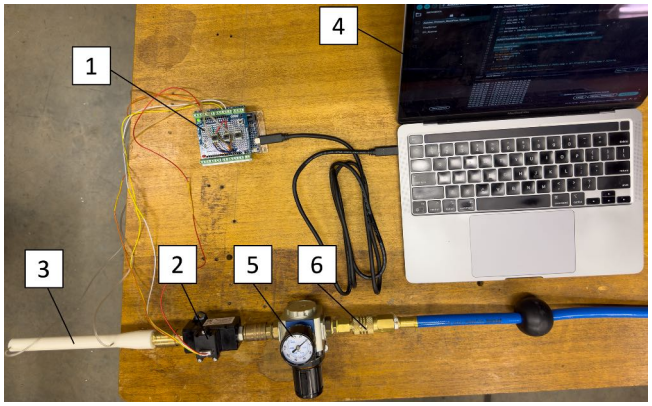

Figure 3 – Nozzle parameter measurement experimental setup
1 - Arduino Uno board with the Honeywell pressure sensors, 2 - Honeywell Mass Flowmeter; 3 - Printed Model;
4 - Laptop; 5 - Pressure regulator; 6 - Air hose connected to compressed air supply

The experimental setup for measuring the nozzle parameters is illustrated in Figure 3. The setup involves connecting an Arduino UNO (1) to pressure sensors and a flowmeter (2). Data are transmitted to a laptop (4) using a USB-C cable. A pressure regulator (5) ensures a consistent pressure and mass flow rate from the compressed air supply (6). The compressed air is directed through a flowmeter to the model (3), which has pressure taps connected to pressure sensors through silicone

tubes. The static pressure recorded at the pressure tap near the flowmeter is denoted as p_1, while the pressure at the tap near the nozzle is denoted as p_2.

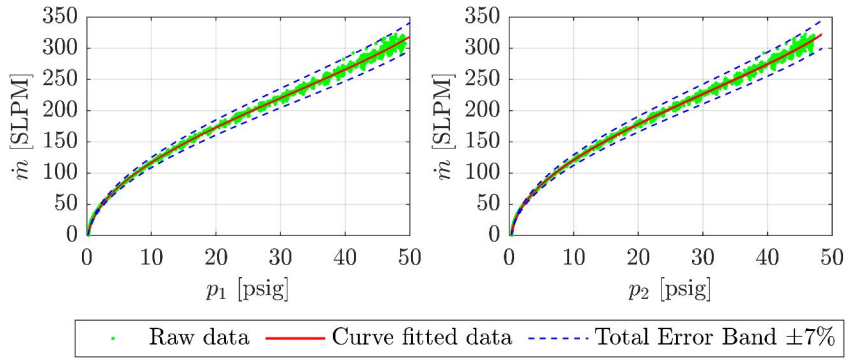

Figure 4 – The variations of the raw data, curve fitted data and TEBs of mass flow rate $\dot{m}$ as functions of static pressure p_1 and p_2

The measurement data were captured for the full range of allowable mass flow rate, from 0 to 300 SLPM. Given that pressure sensors and mass flow metres have total error bands (TEBs) of 1.5% and 7%, respectively, it is expected that the TEB of the measurement will be approximately 7%. The fluctuations of the raw data, the curve-fitted data, and the TEBs of $\dot{m}$ in relation to p_1 and p_2 are shown in Figure 4. It is evident that despite the fluctuations in the collected data, the maximum deviations of the raw data from the curve-fitted data remain within the TEB limit of $\pm 7\%$. This suggests that the instruments used work within specification as defined in the device datasheets [14, 15].

3.2 Conditions for Choked Nozzle

It can also be observed from Figure 4 that when the static pressures p_1 and p_2 are around 15 psi or higher, corresponding to a mass flow rate $\dot{m}$ of around 150 SLPM or higher, $\dot{m}$ changes linearly with p_1 or p_2, indicating that the nozzle is choked under such conditions. This behaviour can be explained by the continuity equation:

$$\dot{m} = \rho AV = \frac{p}{RT} AM\sqrt{\gamma RT} = pAM\sqrt{\frac{\gamma}{RT}} \tag{5}$$

When the nozzle reaches a choked state, the Mach number at any section within the nozzle cannot be raised any further by increasing the pressure. Since the total temperature T_t of the compressed air supply can be considered as a constant, it is safe to assume that the static temperature remains constant or changes only slightly. Therefore, the mass flow rate $\dot{m}$ varies linearly with the static pressure p for any given nozzle section.

Furthermore, the nozzle will be choked if the ratio between the total pressure p_t and the ambient pressure p_a satisfies the following relation [17]:

$$\frac{p_t}{p_\infty} \geq \left(1 + \frac{\gamma - 1}{2}\right)^{\frac{\gamma}{\gamma - 1}} \tag{6}$$

At the time of the nozzle parameter measurements, the ambient conditions were $p_\infty = 101400$ Pa and $T_\infty = 302.3$ K. Given that $\gamma = 1.4$ for air, the condition for a choked nozzle is $p_t/p_\infty \geq 1.89$. With the current configuration, the value of p_t is unknown. However, for a fluid flow, the total pressure p_t is always higher than the static pressure p; therefore, it is safe to say that the nozzle is choked where p_2/p_∞ > 1.89. In this case, p_2 is selected because $p_2 < p_1$ due to the pressure drop through the pipe. Consider that $p_\infty = 101400$ Pa $= 14.7$ psia, the nozzle is choked when $p_2 \geq 28.8$ psia, or $p_2 \geq 14.1$ psig. This result aligns with the observation previously discussed for Figure 4.

3.3 Pressure Drop & Mass Flow Rate Relation

The collected data are now refined to retain only the values where p_2 meets the choked condition. The variation in pressure drop $\Delta p = p_1 - p_2$ for the choked nozzle as a function of mass flow rate $\dot{m}$ is illustrated in Figure 5. It is clear that when the nozzle is choked, Δp varies linearly with respect to $\dot{m}$.

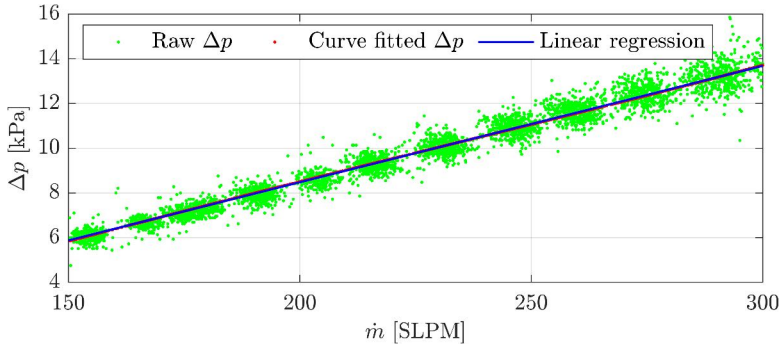

Figure 5 – The variation of pressure drop $\Delta p = p_1 - p_2$ for the choked nozzle as a function of $\dot{m}$

By using the MATLAB function `polyfit` for first degree polynomial, Δp can be written as a function of $\dot{m}$ as:

$$\Delta p = 2.549 \times 10^6 \dot{m} - 1930 \tag{7}$$

It is important to mention that the quantities of Δp and $\dot{m}$ in Equation (7) are provided in SI units (specifically, Δp is in Pa and $\dot{m}$ is in kg/s). In contrast, in Figure 5, $\dot{m}$ is presented in SLPM as it is the direct output from the flowmeter, and Δp is displayed in kPa for better clarity. The relation between pressure drop Δp and mass flow rate $\dot{m}$ can be estimated using the Darcy-Weisbach equation [18]:

$$\Delta p = f_D \left(\frac{L}{d}\right) \rho \frac{V^2}{2} = f_D \left(\frac{L}{d}\right) (\rho A V) \left(\frac{V}{2A}\right) = f_D \left(\frac{L}{d}\right) \dot{m} \left(\frac{M\gamma RT}{2A}\right) \tag{8}$$

When the nozzle reaches choked condition, the Mach number M remains constant as the mass flow rate $\dot{m}$ varies. Since static temperature can be considered as a constant, the change in Δp is only influenced by $\dot{m}$ linearly. This expression is in agreement with the equation provided in Equation (7) and the captured data shown in Figure 5, where the constant value of -1930 Pa can be interpreted as a minor discrepancy between theoretical predictions and experimental observations.

3.4 Estimations of Total Pressure and Total Temperature

Consider the nozzle inlet cross section i where the pressure tap for p_2 is installed. As the nozzle is choked, the Mach number M_i at the cross section 2 with area A_i can be calculated using the area-Mach number relation [17]:

$$\left(\frac{A_i}{A_*}\right)^2 = \frac{1}{M_i^2} \left[\frac{2}{\gamma+1}\left(1 + \frac{\gamma-1}{2} M_i^2\right)\right]^{(\gamma+1)/(\gamma-1)} \tag{9}$$

With A_i/A_* being approximately 3, the Mach number M_2 can be approximated from Equation (9) as $M_i \approx 0.2$. As a result, the total pressure within the nozzle can be determined from p_i ($p_i = p_2$) and M_i:

$$p_t = p_i \left(1 + \frac{\gamma-1}{2} M_i^2\right)^{\frac{\gamma}{\gamma-1}} \tag{10}$$

For temperature terms, the static temperature T_i can be obtained by rearranging Equation (5), and the total temperature can be found with T_i and M_i:

$$T_i = \frac{\gamma}{R}\left(\frac{p_i A_i M_i}{\dot{m}}\right)^2 \qquad\qquad T_t = T_i \left(1 + \frac{\gamma-1}{2} M_i^2\right) \tag{11}$$

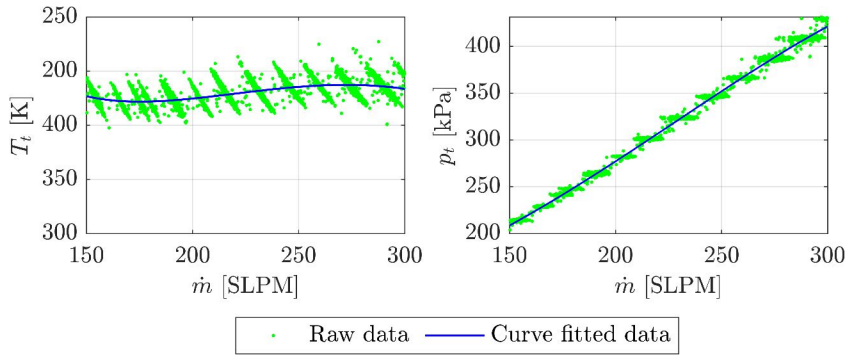

Figure 6 – The variation p_t and T_t as functions of $\dot{m}$ where $\dot{m} \in [150, 300]$ (SLMP)

Changes in p_t and T_t as functions of $\dot{m}$ when $\dot{m}$ increases from 150 to 300 SLMP are illustrated in Figure 6. It can be seen that T_t stays stable around 330 K, as expected, due to the constant total temperature of the compressed air supply. The fluctuations are attributed to the compressor's impact as the compressed air decreases during the tests. Additionally, p_t increases linearly with $\dot{m}$, which is consistent with the linear relationship between static pressure p and mass flow rate $\dot{m}$ under choke conditions.

4. Model Design Finalisation

4.1 Model Scaling

Since the mass flow rate of the model was limited to 300 SLPM as the maximum measurable value of the flowmeter, the model was too small with a base diameter $d_B = 13.4$ mm. This compact size complicates the installation of the air fittings, as illustrated in Figure 3, where it was necessary to enlarge the right end of the model. In addition, a small size also affects the accuracy of the force measurement using the force balance because the force values would be small. Therefore, an initial finding from this design work is any new model needs to be scaled up to a larger size.

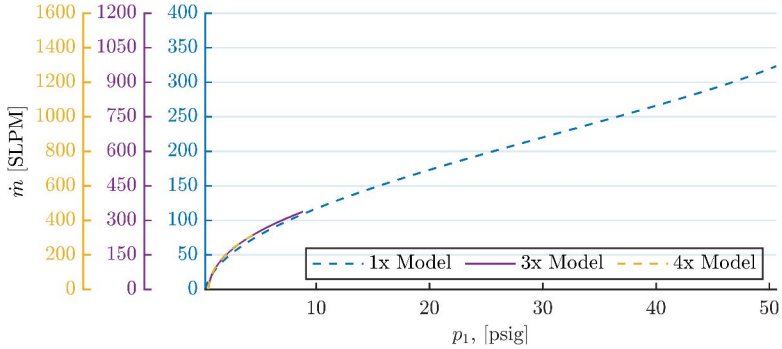

Figure 7 – The relations between p_1 and $\dot{m}$ on the original 1x model and the scaled 3x and 4x models

According to the continuity equation given in Equation (5), scaling the model by a factor of n ($A_{new} = nA_{old}$) implies that the mass flow rate $\dot{m}$ should also be scaled by the same factor n ($\dot{m}_{new} = n\dot{m}_{old}$) to maintain consistent pressure p. To validate this hypothesis, two additional models of identical design were created, scaled by factors $n_1 = 3$ and $n_2 = 4$, respectively. These models were evaluated using the same experimental setup described in Figure 3 to examine the relationship between p_1 and $\dot{m}$ on the original 1x model and the scaled 3x and 4x models.

Figure 7 illustrates the relationship between p_1 and $\dot{m}$ across the three models, with the $\dot{m}$ axis scaled by factors of either 3 or 4. The nearly identical trajectories of the $\dot{m}$ lines suggest that for a given p_1, scaling the model by n results in a proportional scaling of the mass flow rate $\dot{m}$ by n. Minor variations among these $\dot{m}$ lines are likely due to the varying ratios of boundary layer thickness to channel

diameter, with the ratio in the 1x model being higher than that in the 3x and 4x models. Further tests focused on measuring the maximum static pressure attainable for scaled models. The 3x model achieved approximately 20 psi, while the 4x model reached about 13.5 psi. Consequently, the 3x model was selected as the final wind tunnel model due to its ability to ensure choked nozzle conditions and broader pressure capabilities.

For the selected design point $p_1 = 20$ psig, the final design parameters are derived with the same method discussed in previous sections with a scale factor $n = 3$ applied for $\dot{m}$, resulting in $\dot{m} = 534$ SLPM, $T_t = 330$ K, and $p_t = 245,900$ Pa. Using these values, the final design geometry was determined with a throat diameter of 5 mm, a nozzle expansion ratio of 1.115, and a base diameter of 21 mm. The primary parameters for the testing conditions of this final design are detailed in Table 2, along with a comparison to the flight conditions.

Condition	C_T [–]	APR [–]	V_∞ [m/s]	p_∞ [Pa]	T_∞ [K]	ε [–]	p_e [Pa]	M_e [–]	T_e [K]
Flight	124.4	0.762	32.2	100300	287.5	16	76460	3.521	1810
Testing	124.4	0.762	15.2	101400	302	1.115	77320	1.40	237

Table 2 – The main parameters of the flight and testing conditions for the final design

Table 2 shows that the key retropropulsion similarity parameters C_T and APR in the testing conditions match those in the flight conditions. The freestream velocity $V_\infty = 15.16$ m/s for the tests falls within the wind tunnel's operational limits. Moreover, the values of nozzle exit pressure p_e and temperature T_e are adequate and appropriate to avoid condensation. Therefore, the final design satisfies all requirements and is ready to advance to the final manufacturing phase.

4.2 Final Design

The drawing of the final design is shown in Figure 8. In this study, the final model represents a simplified version of the RFZ vehicle, consisting of a cylindrical body of 300mm in length and 21mm in diameter. The design divides the model into two parts, the nozzle part and the mounting part, to accommodate the dimensions of the available 3D printer.

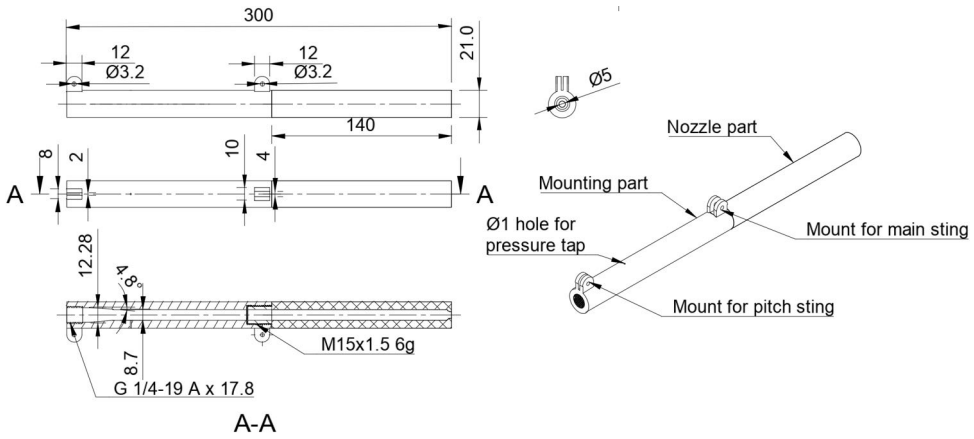

Figure 8 – The drawing of the model final design (all dimensions are in mm)

The nozzle section, 140mm in length, includes a nozzle near the right end and an 8.7mm diameter channel that leads to it. Conversely, the mounting section is 160mm long and incorporates a G-1/4 inch thread for the air fitting at its left end. The internal channel starts wider at the left end to fit the air fitting and tapers to a channel of 8.7mm in diameter. In addition, the model features a 1mm diameter hole for a pressure tap to monitor static pressure p_1 within the channel, while static pressure p_2 is obtained from Equation (7). The mounting part also features two sting mounts: one for the main sting connected to the overhead balance for aerodynamic force measurements, and another for the pitch sting that can be used to adjust the angle of attack. It is worth noting that the main sting mount

is positioned near the model's center of gravity to enhance the measurement accuracy and reduce moments. The printed model in one of the wind tunnel configuration is given in Figure 9.

Figure 9 – Wind tunnel setup with the printed model

5. Numerical Setup

The TAU code is a second order finite-volume solver for the Euler and Navier-Stokes equations which includes a comprehensive range of RANS-based or scale resolving turbulence models. It uses unstructured computational grids to facilitate the analysis of complex geometries and is highly optimised for the application on massively parallel HPC systems. TAU has been successfully applied to a wide range of sub-to-hypersonic flow problems, both in scientific and industrial applications, including the analysis of reusable launcher configurations.

Turbulence was modelled using the two equation k-ω SST model from Menter. The single equation S-A turbulence model has been found to be very effective in replicating the plume structure during cases modelling hypersonic retro-propulsion maneouvres [19, 20], however, it has been shown that it results in a short plume length in the subsonic regime [21]. An adequate setup of the numerical grid is required which is achieved by using prismatic sub-layers close to the wall with a first dimensionless wall spacing of y+ in the order of one and a wall normal stretching ratio of grid cells of less than 1.3. As the simulations are based on the wind tunnel experiments to be conducted with compressed air modelling the plume in a continuously run subsonic facility, the walls are set to be adiabatic. The compressed and freestream air are considered to have a ratio of specific heats of 1.4.

The mesh exploits the simple geometry of the wind tunnel model and represented using a 2D axisymmetric grid. The mesh contains approximately 550 thousand grid points. The domain extends approximately 3 metres radially, upstream of the nozzle and downstream of the rear portion of the model. A region of mesh refinement has been used to better capture the flow phenomena around the vehicle, with further refinement placed directly at the nozzle exit to better resolve the plume. This setup does not account for the wind tunnel walls, however due to the small size of the model compared to the test section, it is assumed that the presence of the walls will have little to no influence on the results.

The inputs for the CFD computations were based on those measured during the experimental campaign. A reservoir pressure inflow boundary condition was used to model the compressed air line, with a total temperature of 330 K and total pressure of 245900 Pa. For the subsonic counterflow a static pressure in the test section of 101400 Pa was used with a static temperature of 302 K. The airspeed in the wind tunnel was 15.2 m/s. The wall temperature is set to be adiabatic.

6. CFD Results

Initial numerical results highlight that a maximum Mach number in the jet of 1.32 is realised, which agrees well with initial design estimates dervied using isentropic relations. Figure 10 highlights the overexpanded plume structure, which was expected based on the ambient pressure ratio of this

nozzle. The variance in Mach number is a result of flow expansion and compression, as the pressure in the jet attempts to equalise with the ambient pressure in the test section.

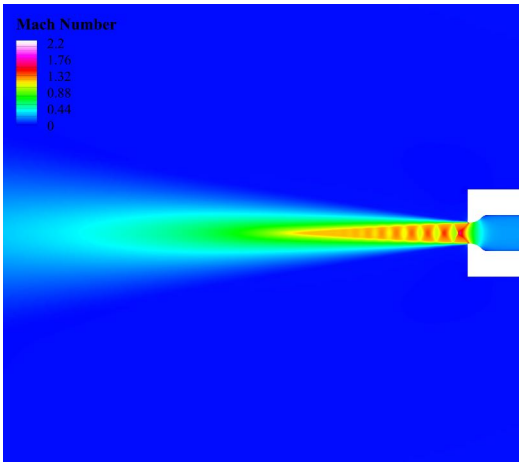

Figure 10 – Mach contours highlighting the classical overexpanded plume structure

Figure 11 shows the jet penetration length to be approximately 0.47 metres and large regions of recirculating flow appear along the plume, which extend radially by 0.12 metres. This is due to the stagnation of the flow where the freestream meets the jet, before it is redirected towards the baseplate of the model.

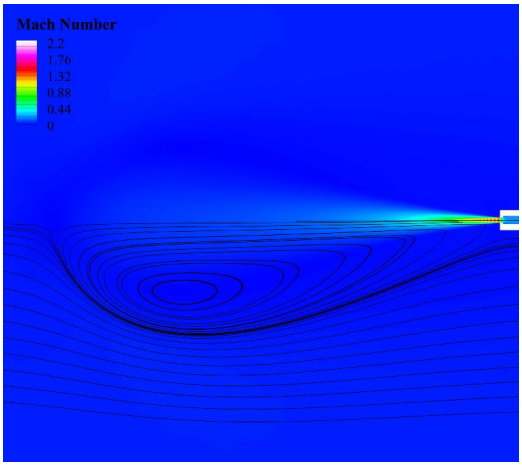

Figure 11 – Mach contours with streamlines highlighting jet penetration length and regions of recirculating flow

7. Conclusions and Future Work

The paper has designed an aerodynamic model for a reusable launch vehicle (RLV) during its final descent phase. Following several design iterations, the model was completed with carefully scaled nozzle parameters, ensuring supersonic flow at the nozzle's exit while maintaining similarity with the RFZ vehicle. For this purpose, a system of measurement devices was developed to precisely measure the high-pressure environments in the nozzle flow. The final model features a nozzle throat diameter of 5 mm, an expansion ratio of 1.115, a base diameter of 21 mm, and a length of 300 mm. CFD simulations verified that a supersonic jet is achieved and revealed a large recircultion region along the length of the plume, penetrating into the freestream 5.7 base plate diameters radially and 22.4 diameters axially. This work has formed the foundation for future investigations which will look at increasing the available reservoir pressure to enable upscaling of the model.

Contact Author

Email: ahoa4149@uni.sydney.edu.au

Copyright Statement

References

[1] Carmichael S. *Moon Men Return: USS Hornet and the Recovery of the Apollo 11 Astronauts*. Naval Institute Press, 2010.

[2] Jones H. The Recent Large Reduction in Space Launch Cost. *48th International Conference on Environmental Systems*, 2018.

[3] Seedhouse E. *SpaceX: Starship to Mars - the First 20 Years*. Springer Praxis Books, Cham, Switzerland, 2nd edition, 2022.

[4] Klevanski J, Ecker T, Riehmer J, Reimann B, Dumont E, and Chavagnac C. Aerodynamic Studies in Preparation for CALLISTO - Reusable VTVL Launcher First Stage Demonstrator. In *69th International Astronautical Congress (IAC)*, Bremen, Germany, 2018.

[5] Bykerk T. A standard model for the investigation of aerodynamic and aerothermal loads on a re-usable launch vehicle. In *10th EUCASS - 9th CEAS 2023*, Lausanne, Switzerland, 2023.

[6] Gutsche K, Marwege A, and Gülhan A. Similarity and Key Parameters of Retropropulsion Assisted Deceleration in Hypersonic Wind Tunnels. *Journal of Spacecraft and Rockets*, 58(4):984–996, 2021.

[7] Jarvinen P. O and Adams R. H. The aerodynamic characteristics of large angled cones with retrorockets. Contractor Report NAS 7 - 576, NASA, 1970.

[8] El-Sayed A. F. *Fundamentals of Aircraft and Rocket Propulsion*. Springer London : Imprint: Springer, London, UK, 1st ed. 2016 edition, 2016.

[9] Sforza P. M. *Theory of Aerospace Propulsion*. Elsevier Aerospace Engineering Series. Elsevier, second edition edition.

[10] Rfz-Model. Data of the RFZ Model - A standard model for the investigation of aerodynamic and aerothermal loads on a re-usable launch vehicle. Zenodo, July 2023.

[11] Anderson J. D. *Fundamentals of Aerodynamics*. McGraw-Hill Series in Aeronautical and Aerospace Engineering. McGraw Hill Education, New York, NY, sixth edition.

[12] Wegener P and Mack L. Condensation in Supersonic and Hypersonic Wind Tunnels. In *Advances in Applied Mechanics*, volume 5, pages 307–447. Elsevier, 1958.

[13] MPS4264 - Miniature Pressure Scanner.

[14] Honeywell. HAF SERIES Datasheet - Honeywell Zephy Digital Airflow Sensors.

[15] Honeywell. ABP2 SERIES Datasheet - Board Mount Pressure Sensors.

[16] Arduino. Arduino UNO R4 Minima Datasheet.

[17] Anderson J. D. *Modern Compressible Flow: With Historical Perspective*. McGraw Hill, fourth edition edition.

[18] Howell G. W, Weathers T. M, and CA T. S. G. R. B. Aerospace fluid component designers' handbook, volume II, Revision D.

[19] Bykerk T, Fechter S, Kirchheck D, and Karl S. Condensation modelling of expanding cold gas jets during hypersonic retro-propulsion manouvres within the retpro project. In *The 23rd Australasian Fluid Mechanics Conference (23AFMC)*, December 2022.

[20] Bykerk T, Kirchheck D, and Karl S. Reconstruction of wind tunnel tests using cfd for a reusable first stage during rocket retro- propulsion. In *9th European Conference for Aeronautics and AeroSpace Sciences (EUCASS)*, July 2022.

[21] Ertl M, Ecker T, amd E. Dumont J. K, and Krummen S. Aerothermal analysis of plume interaction with deployed landing legs of the callisto vehicle. In *9TH EUROPEAN CONFERENCE FOR AERONAUTICS AND AEROSPACE SCIENCES (EUCASS)*, July 2022.